J. Space Weather Space Clim. 2023, **13**, 1

https://doi.org/10.1051/swsc/2022038

JSWSC

Available online at:
www.swsc-journal.org

Topical Issue - Ionospheric plasma irregularities and their impact on radio systems

RESEARCH ARTICLE OPEN ACCESS

Ionospheric plasma structuring in relation to auroral particle precipitation

Florine Enengl*, Daria Kotova, Yaqi Jin, Lasse B.N. Clausen, and Wojciech J. Miloch

Department of Physics, University of Oslo, Problemveien 7, 0315 Oslo, Norway

Received 11 May 2022 / Accepted 29 November 2022

Abstract – Auroral particle precipitation potentially plays the main role in ionospheric plasma structuring. The impact of auroral particle precipitation on plasma structuring is investigated using multi-point measurements from scintillation receivers and all-sky cameras from Longyearbyen, Ny-Ålesund, and Hornsund on Svalbard. This provides us with the unique possibility of studying the spatial and temporal dynamics of the aurora. Here we consider three case studies to investigate how plasma structuring is related to different auroral forms. We demonstrate that plasma structuring impacting the GNSS signals is largest at the edges of auroral forms. Here we studied two stable arcs, two dynamic auroral bands, and a spiral. Specifically for arcs, we find elevated phase scintillation index values at the poleward edge of the aurora. This is observed for auroral oxygen emissions (557.7 nm) at 150 km in the ionospheric E-region. This altitude is also used as the ionospheric piercing point for the GNSS signals as the observations remain the same regardless of different satellite elevations and azimuths. Further, there may be a time delay between the temporal evolution of aurora (e.g., commencement and fading of auroral activity) and observations of elevated phase scintillation index values. The time delay could be explained by the intense influx of particles, which increases the plasma density and causes recombination to carry on longer, which may lead to a persistence of structures – a "memory effect". High values of phase scintillation index values can be observed even shortly after strong visible aurora and can then remain significant at low intensities of the aurora.

Keywords: Particle precipitation / Phase Scintillation Index / Auroral plasma structuring / Ionospheric E-region

1 Introduction

The aurora can be seen as the signature of direct coupling between the ionosphere and magnetosphere. During the high geomagnetic activity, energetic particle precipitation leads to higher intensity of the aurora resulting in different auroral forms. Dynamical processes in the E- and F-regions of the ionosphere are often associated with instabilities and turbulence which result in plasma structuring and irregularities at various scales. Such irregularities in ionospheric plasma density have an impact on the propagation of radio waves (e.g., Keskinen & Ossakow, 1983; Huba et al., 1985; Kintner & Seyler, 1985; Moen et al., 2013; Deshpande et al., 2014). Trans-ionospheric radio waves propagating through regions with density irregularities undergo diffraction and refraction, and they result in rapid fluctuations in phase and amplitude of the received signal, referred to as scintillation (e.g., Hey et al., 1946; Kintner et al., 2007). Scintillation of the received signal affects man-made systems, such as radio communication and/or satellite-based positioning systems. At the same time, scintillation of the received signal can be used as an indication for ionospheric plasma structuring. This will be also the approach in this work, where we will focus on the role of the auroral particle precipitation during geomagnetic substorms and investigate how different discrete auroral forms, i.e., stable arcs and fast-moving forms (such as spirals), relate spatially and temporally to structuring in the ionospheric plasma density.

The Earth's ionosphere and magnetosphere are directly coupled in the polar regions via the Birkeland currents, which can be seen as drivers for the aurora. There is a variety of resulting auroral forms, which have been categorized over many years with regard to their shapes, process, and lifetime, but to this day there is no clear and well-accepted definition for all of the forms. Some auroral forms and their evolution can be linked to certain substorm phases (e.g., Akasofu, 1966; Elphinstone et al., 1996; Partamies et al., 2015). The auroral arcs are well-studied phenomena in quiet (for a review see Karlsson et al., 2020) and active geomagnetic periods. Davis (1978) studied auroral arcs and their distortions into complex forms (spirals and curls) and defined an auroral arc as a recognizable luminosity resulting from the impingement of a field-aligned sheet beam of charged particles upon the atmosphere. The most simple form is an east-west elongated quiet discrete

*Corresponding author: florine.enengl@fys.uio.no

auroral arc. The width of the arc can be very thin (0.5–1.5 km) (Partamies et al., 2010), but most mesoscale-size arcs have an observed width of around 10–50 km (Knudsen et al., 2001).

Arcs often appear in multiple-arc structures and are found both during quiet and active periods. Multiple arc structures are arrays of arcs that are near-parallel to each other and in close proximity, and they are also the most common form of discrete auroral observations (Davis, 1978; Gillies et al., 2014). The multiple arc structures are referred to as arc packets when they are formed by splitting the trailing arc into two, possibly due to the Alfvén wave dispersion (Semeter et al., 2009). Stable and quiet auroral arcs are expected in the evening and at nighttime. Here, we will study auroral emissions in the night time sector from 21:00 to 03:00 MLT (magnetic local time).

Other notable auroral distortions are curl, spiral, bands, ray forms, westward traveling surge or omega bands (e.g., Hallinan & Davis, 1970; Elphinstone et al., 1996; Ivchenko et al., 2005; Partamies et al., 2017). In this paper, we will focus on spiral structures. Spirals are larger-scale auroral vertices (20–1300 km), which form as the aurora twists counter-clockwise. It is suggested that the Kelvin-Helmholtz instability could play a role in the formation of the spiral (Hallinan & Davis, 1970; Davis & Hallinan, 1976; Hallinan, 1976; Partamies et al., 2001). While Davis and Hallinan (1976) and Keiling et al. (2009) relate spirals to magnetically disturbed periods, Partamies et al. (2001) relate them primarily to magnetically quiet conditions. However, fast-moving spirals, whose signatures are only found in a single all-sky camera (ASC) image, seem to be related to increasing geomagnetic activity Partamies et al. (2001).

A variety of highly dynamic phenomena (e.g., polar cap patches, field-aligned currents, high-density F-region plasma, or particle precipitation) cause plasma irregularities in the E- and F-regions ionosphere (e.g., Moen et al., 2013; van der Meeren et al., 2015; Jin et al., 2016, 2017; Spogli et al., 2016; Fæhn Follestad et al., 2020). Ionospheric plasma structuring can be indirectly observed by scintillation receivers. Recorded signals allow for calculating the phase and amplitude scintillation index values. At high latitudes, the effect of irregularities on the trans-ionospheric wave can also be reflected in the degradation of the receiver tracking performance, Total Electron Content (TEC) jumps, and cycle slips (Skone et al., 2001; Alfonsi et al., 2008; Moen et al., 2013; Chernyshov et al., 2020; references therein).

Auroral particle precipitation can lead to significant plasma irregularities (Kelley et al., 1982; Keskinen & Ossakow, 1983; Weber et al., 1985; Prikryl et al., 2011), but it is still an open question to what extent it contributes to plasma structuring and whether it is dominant in the E or F-region ionosphere. It is observed that soft particle precipitation is unlikely to be the main source of the large-scale F-region plasma structures on the nightside (Jin et al., 2016). While on the dayside the main ionization source of the E-region is the EUV solar radiation, on the nightside Joule heating and auroral particles with energies of 10–30 keV dominate the energy input into the system (Millward et al., 1999; Wilson et al., 2006; Nikolaeva et al., 2021).

There have been previous studies that tried to answer this question. Kinrade et al. (2013) studied ionospheric irregularities caused by the auroral particle precipitation using scintillation receivers and auroral imagers located at the South Pole. They found spatially and temporally well-correlated scintillations with atomic oxygen emissions at wavelengths of λ = 557.7 nm and 630.0 nm. This correlation is better for emissions at λ = 557.7 nm, which could be due to the tracking method's effectiveness at two emission wavelengths of different characteristic intensities. They found optical images of aurorae to be a useful spatial and temporal indicator of the GPS phase scintillations during intense and persistent auroral activity, especially for discrete arcs and at the auroral boundary. Another study, by van der Meeren et al. (2015), sheds light on the Global Navigation Satellite System's (GNSS's) signal scintillations during intense substorm aurora. The data was recorded at GNSS receivers around Svalbard. They observed severe phase scintillation, which was following the intense poleward edge of the auroral oval as it expanded poleward and showed that received signals may experience strong scintillation when they intersect oxygen (λ = 557.7 nm) emissions. The satellite systems of GPS, GLONASS, and Galileo were affected similarly through the scintillations in relation to the intense line of sight auroral emissions in a highly localized region of the sky. Discrete aurora and GPS signal corruption have been studied by Semeter et al. (2017), using a network of receivers and imagers in Alaska. The ASC sampled images of oxygen emissions at λ = 558 nm. The auroral form of interest was a westward traveling surge and the loss of lock events consistently appeared at the edges of auroral forms. The scintillation regions were confined to a narrow strip (<20 km) tangential to the trailing edge of the observed aurora. As the appearance of the loss of lock events consistently followed the auroral boundaries irrespective of the satellite elevation and azimuth, the authors suggested the source to be near the oxygen 558 nm emission line. This is within the E-region of the ionosphere. A consequent study from Mrak et al. (2018), using co-located GPS-ASI sensors in Alaska to remove mapping ambiguity, concludes that E-region electrodynamic processes are sources of plasma irregularities.

The following two questions remain open: i) in which layer of the ionosphere does the auroral particle precipitation play a dominant role in plasma structuring? ii) what spatial and temporal characteristics of the enhanced scintillation index values relate to which auroral forms? In this paper, we will study how stable auroral arcs and fast-moving forms (bands and spirals) relate spatially and temporally to ionospheric plasma structuring. The observations are made by using several scintillation receivers and ASCs located in Longyearbyen, Ny-Ålesund, and Hornsund on Svalbard. Case studies that consider different auroral forms during the substorm events are presented. We observe elevated values of the phase scintillation index poleward of the arcs, and at the boundaries of fast-moving forms. These characteristics have been found for the 557.7 nm oxygen emissions, indicating that the auroral particle precipitation in the E-region can contribute to relevant plasma structuring. We also observe a short time delay between the onset of the aurora and observed plasma structuring.

2 Instruments and approach

To study whether plasma structuring is driven by particle precipitation, we investigate the relative location between elevated scintillation index values and the aurorae. For this purpose, we use data from three ASC on Svalbard. Two of the cameras are Keo Sentry 4ix Monochromatic Imagers from

KEO Scientific, with filters, operated by the University of Oslo (UiO). They are situated in Longyearbyen (LYR, geographic coordinates: 78.15° N, 16.04° E), and in Ny-Ålesund (NYA, geographic coordinates 78.92° N, 11.93° E). The imagers record emission intensities every 30 s, with a field of view (FOV) of 180°. Both imagers are equipped with narrowband filters to monitor 557.7 nm (green) and 630.0 nm (red) auroral emissions. For the analysis, the ASC images are projected to 150 km and 250 km (green and red auroral emission altitudes) respectively. The imager in Hornsund (HOR, geographic coordinates 77° N, 15.55° E) is a Sony A7 SII color camera with a FOV of 180, also operated by UiO. The availability of recorded images for this camera on the days of interest is every 15 min. The ASCs are used to determine the form of the aurora and its relative location to the observed elevated scintillation index values of Global Navigation Satellite Systems (GNSS) signals.

To analyze the impact of auroral particle precipitation on the GNSS signals, five GNSS ionospheric scintillation receivers on Svalbard are used in this study. The delay Δt of a signal propagating through a plasma is dependent on the electron density n_e and the signal frequency f:

$$\Delta t = \frac{40.3}{cf^2} \int n_e \mathrm{d}\rho, \tag{1}$$

with c being the speed of light, ρ the ray path (e.g., Kintner et al., 2005, 2007).

The phase ϕ is connected to time delay Δt and therefore to electron density variations along the signal path (Eq. (1)) through

$$\phi = f\Delta t, \tag{2}$$

(e.g., Yeh & Liu, 1982; Kintner et al., 2007). As the phase is affected by the time delay and electron content variations it indicates plasma structuring processes. Phase fluctuations are caused by irregularities covering the full range of scales from meters to a few kilometers (e.g., Basu et al., 1998; Kintner et al., 2007). The phase scintillation index σ_ϕ,

$$\sigma_\phi = \langle \phi^2 \rangle - \langle \phi \rangle^2, \tag{3}$$

is the standard deviation of the detrended measured phase and is dominated by large-scale fluctuations (Yeh & Liu, 1982; Kintner et al., 2007). Even though the index is not issue-free, for example, due to the dominance of the low-frequency component of the phase power spectrum, the phase or related electron density variations nevertheless can indicate physical structuring in the ionosphere (Beach, 2006). Refractive and diffractive variations of σ_ϕ are not differentiated in this study, as we use σ_ϕ as a measure of plasma structuring and to study the relative location to auroral forms, but are not studying the effects on the carrier phase. Amplitude scintillations are described by the amplitude scintillation index S_4:

$$S_4 = \sqrt{\frac{\langle I^2 \rangle - \langle I \rangle^2}{\langle I \rangle^2}}, \tag{4}$$

with I being the signal intensity (e.g., Briggs & Parkin, 1963; Yeh & Liu, 1982). The S_4 index describes and is affected by irregularities in a range of hundreds of meters to meters (at and below the Fresnel radius) (e.g., Basu et al., 1998; Kintner et al., 2007).

In this study, we use the calibrated 60-second reduced data (Oksavik, 2020a) of the phase (σ_ϕ) and amplitude (S_4) scintillation index. A cut-off angle of 15° is applied to the scintillation data to minimize multipath effects.

The data is recorded by NovAtel GPStation-6 receivers. The receiver in Hornsund is situated about 500 m from the ASC and is run by the University of Oslo. The receivers situated in Ny-Ålesund (co-located with the NYA ASC), Longyearbyen (co-located with the LYR ASC), Bjørnøya (BJN, geographic coordinates 74.50° N, 19° E), and Hopen (HOP, geographic coordinates 76.51° N, 25.01° E) are operated by the University of Bergen (Oksavik, 2020b). The receivers track GPS, Galileo, and GLONASS satellites. We use all received signals (GPS: L1CA, L2Y, L2C, L2P, L5Q; GLONASS: L1CA, L2CA, L2P; GALILEO: E1, E5A, E5B, E6) as they have previously been shown to be similarly affected by ionospheric irregularities (van der Meeren et al., 2015; Alfonsi et al., 2016).

The Interplanetary Magnetic Field (IMF) data and the solar wind conditions are downloaded from NASA/GSFC's OMNI data set through OMNIWeb (King & Papitashvili, 2005). We assess the IMF Bz magnetic field component, the solar wind flow speed, and sym-H (1-min resolution GSM (geocentric solar magnetospheric coordinates) data). A negative IMF Bz component can indicate dayside reconnection. The sym-H index is a measure of the magnetospheric ring current intensity and is used to quantify geomagnetic storms. The index is calculated using data from different magnetometer stations near the equator and describes the symmetric part of the magnetic field horizontal component (Wanliss & Showalter, 2006). These indices help to describe and filter for background conditions and evaluate whether the geomagnetic conditions indicate geomagnetic storms. To investigate substorm conditions the horizontal component of the local magnetic field was used. It is recorded by a magnetometer network around Svalbard operated by the Tromsø Geophysical Observatory (Tanskanen, 2009). The decrease in the B_x component of the magnetic field at high latitudes is a signature of the enhancement of the westward electrojet and the substorm current wedge in superposition with eastward electrojet enhancements (Akasofu, 1965; D'Onofrio et al., 2014). Further, we use the Kp index (from GFZ Potsdam and the National Geophysical Data Center), which is a proxy for the energy input from the solar wind to the magnetosphere. The Kp index is calculated based on 13 selected subauroral ground-based magnetic observatories and is the mean value of the disturbance levels in the horizontal magnetic field components. Higher Kp values correspond to stronger disturbances (Matzka et al., 2021).

3 Case selection and conditions

Data from the ASC network were used to select events for the case study. The first season (2019/2020) when all three cameras (NYA, LYR, HOR) were in operation and recorded data, is considered for this study. The season spans from October-March. On 73 days all three ASCs have recorded data in an overlapping timespan (2 h). Days with Kp < 5 were excluded. This reduced the set to 24 days. The solar wind conditions for each of the selected events are shown in Figure 1. Most of these days are part of six longer lasting multi-day (5+ days) moderate geomagnetic storm events with high solar wind

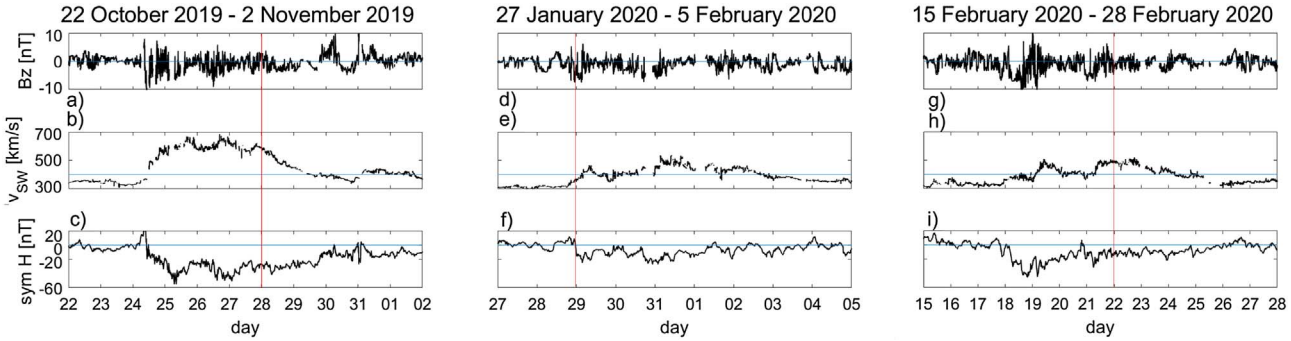

Fig. 1. Solar wind data recorded during the selected case study dates: 28 October 2019 (a–c), 29 January 2020 (d–f), and 22 February 2020 (g–i), indicated by red vertical lines. Panels a, d, and g show the solar wind/interplanetary magnetic field Bz component, indicating reconnection with Earth's magnetic field when negative. Panels b, e, and h show the solar wind flow speed that during geomagnetic storms increases to over 400 km/s, as indicated by a horizontal line, while the sym-H component (a measure of the ring current), shown in panels c, f, and i abruptly goes negative during storms with a change of sym $H > 20$ nT (here the horizontal line corresponds to zero).

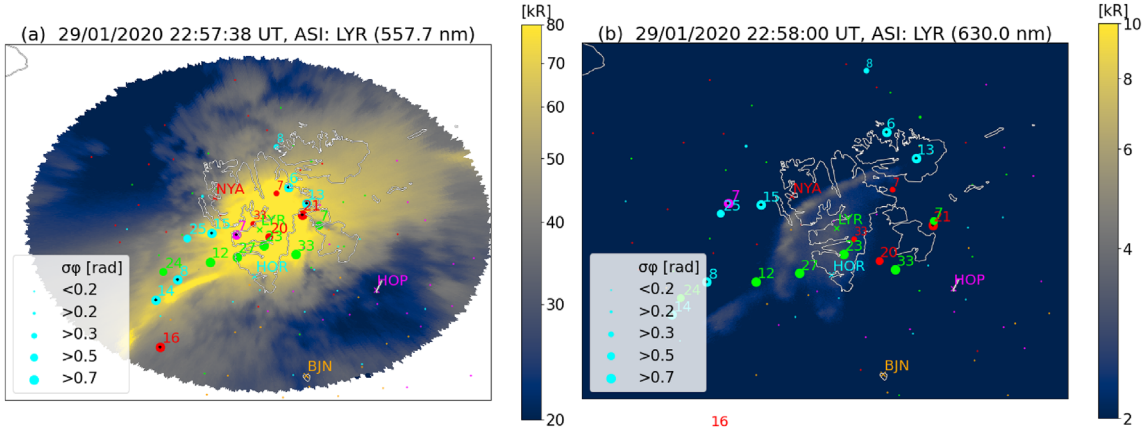

Fig. 2. The projection of the 557.7 nm (panel a)/630.0 nm (panel b) emissions shown together with the phase scintillation index σ_ϕ over a map of Svalbard on 29 January 2020 as seen from the LYR ASC. Brighter yellow auroral emissions mean stronger intensity and bigger markers mean stronger σ_ϕ. The markers represent σ_ϕ measurements from NYA in red, LYR in green, HOR in cyan, HOP in magenta, and BJN in orange. While the elevated σ_ϕ follow the shape of the 557.7 nm auroral emissions shown in panel a, they are observed displaced with regards to the 630.0 nm auroral emissions shown in panel b.

speeds (above 400 km/s; see Figs. 1b, 1e, 1h), negative sym-H component (−20 nT to −40 nT; see Figs. 1c, 1f, 1i), re-occurring negative Bz (see Figs. 1a, 1d, 1g) and negative drops of the local B_x component (shown in Figs. 3a, 3e, 3i). For comparability of the cases events with available data between 18:00 and 20:00 UT (21:00–03:00 MLT nightside) were selected, which means the data set has been reduced to find times at which all three ASC recorded continuous data in the majority of the 18:00–24:00 UT section. The set is now down-filtered to 12 days as the remaining candidates for the case study. After the filtering process, the imagery was visually assessed and out of the days with intense auroral emissions, the days with the least cloud cover (for all three ASC) that were part of different geomagnetic storm events were selected. The selected dates are 28 October 2019, 29 January 2020, and 22 February 2020. The similarity in the events lies in the background conditions as all selected dates are substorm events with Kp > 5. The events are in the night sector to meet similar geomagnetic conditions and types of aurora. Particle precipitation is strongly visible on all of them. The randomness in the case study events is achieved through limited data availability and cloud cover on the ASC images, providing us with a representative set of case studies with similar conditions, but spread over the whole season.

4 Observations

Figure 3 shows data from the selected case study dates: 28 October 2019, 29 January 2020, and 22 February 2020 from 18:00 to 24:00 UT. In Figures 3a, 3e, and 3i the horizontal magnetic field component B_x is shown. The decreases in B_x indicate substorm events at the respective stations (NYA-red, LYR-green, HOP-black, BJN-orange, HOR-blue). Times of intense particle precipitation can be investigated by presenting the center pixel column of the ASC images as a time series – this time versus latitude plot is named a keogram. The keograms reveal times of auroral activity above the zenith of the recording ASC. The keograms presented in Figures 3b, 3f, and 3j show images that originate from the LYR ASC using the filter for

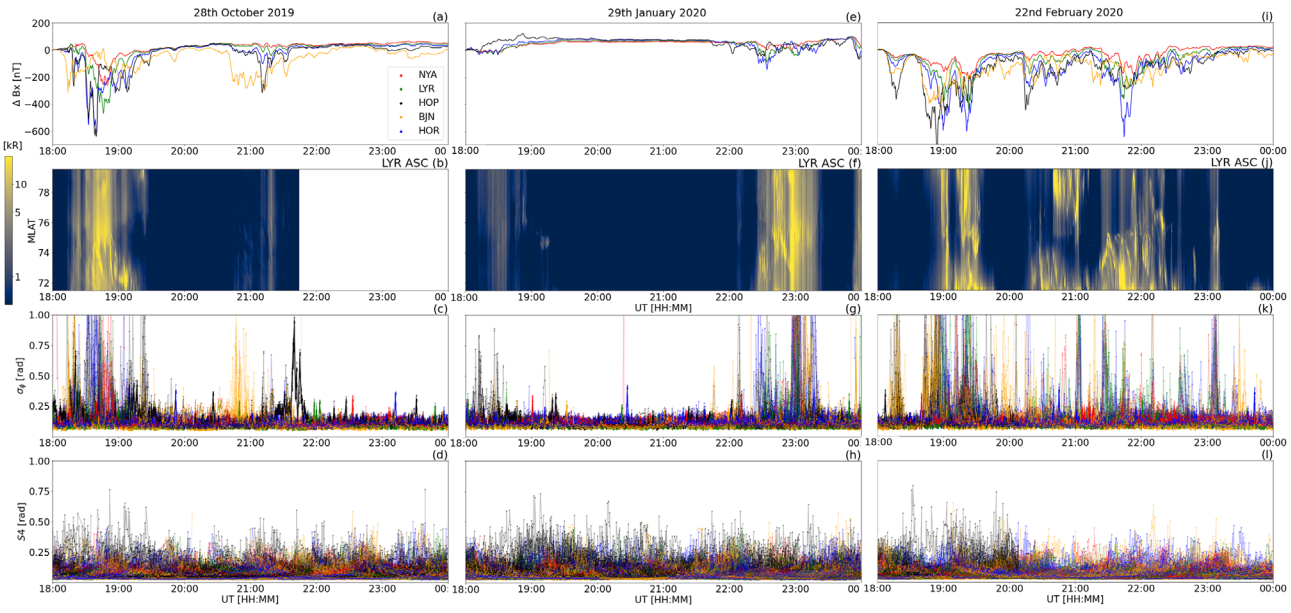

Fig. 3. Data from the selected events: 28 October 2019, 29 January 2020, and 22 February 2020 from 18:00 to 24:00 UT. In panels a, e, and i, the horizontal magnetic field component B_x is shown. The dips indicate substorm events at the respective stations (NYA – red, LYR – green, HOP – black, BJN – orange, HOR – blue). Panels b, f, and j show the 557.7 nm emissions intensity observed by the LYR ASC in form of a keogram. The bright auroral emissions correspond to times of particle precipitation. Panels c, g, k and d, h, l show σ_ϕ and S_4 scintillation index data recorded by the scintillation receivers in the respective stations. They quantify the location, scale, and intensity of plasma structuring.

557.7 nm (green) emissions. Here we associate the auroral activity, visible bright auroral emissions, with times of particle precipitation. Figures 3c, 3g, 3k and 3d, 3h, 3l show σ_ϕ and S_4 scintillation index data recorded by the scintillation receivers in the respective stations. The indices are used to quantify plasma structuring in location, intensity, and scale. The S_4-index indicates plasma structuring on scales down to a few meters, below the Fresnel radius, while σ_ϕ indicates structuring above the Fresnel radius (hundreds of meters to km).

4.1 Altitude of plasma structuring

Different regions in the ionosphere are influenced by different phenomena characteristic of the specific altitude ranges. Determining the altitude which the GNSS signals are disrupted is crucial to relate the disturbances observed through the phase scintillation index to physical phenomena. To answer in which layer of the ionosphere the auroral particle precipitation plays a dominant role in plasma structuring, we evaluate whether elevated σ_ϕ corresponds better to red or green auroral emissions and at what mapping altitude the auroral evolution corresponds best to elevated σ_ϕ. In order to do so, we first establish whether the elevated σ_ϕ corresponds to aurorae and if so to which wavelength (Step 1). Then we discuss the mapping ambiguity and why we can project all data (ASC and scintillation receivers) to the same altitude (Step 2).

Step 1: The images of green and red auroral emissions are projected to their estimated emission altitudes (150 km and 250 km respectively). The scintillation index values are projected to different altitudes (piercing points) to find out whether the observed disturbances happen in the same altitude range as the auroral emissions and whether they correspond better to the green or red emissions. For this, different piercing points between 100 km to 350 km were tested, while the auroral emission projections were kept constant at their respective estimated altitudes. For the green auroral emissions (150 km), it is observed that for lower (100 km) or higher (200 km) piercing point altitudes, the elevated σ_ϕ values appear randomly placed with regards to the auroral forms. When observing small patches of auroral emissions further east/west of zenith, one observes the elevated σ_ϕ values further east/west of the patch when the ionospheric piercing point is chosen low/high. However, when choosing the green auroral emission altitude as the altitude of the piercing points, we find that the elevated σ_ϕ values occur at the boundaries and align well with the evolution of auroral forms. Using imagery from all three ASC and all five receivers, elevated σ_ϕ values are consistently found at the edges of the auroral forms for this piercing point altitude. This indicates that the signal is impacted right at the altitude of green auroral emission. This pattern has not been detected to the same extent with regards to red auroral emissions, see an example in Figure 2 and Videos (S1 – green emissions; S2 – red emissions) in the supplementary material.

This behavior is observed for chosen piercing points for satellites regardless of satellite azimuth or elevation, just as in Semeter et al. (2017). The elevated σ_ϕ values are increased at the boundaries of the auroral emissions, invariant with different satellite elevations. However, as we do not use the magnetic field inclination or orientation, this is not our main reason for allowing the projection of all data from different receivers to the same altitude.

Step 2: Better evidence to use the green auroral emission altitude as a piercing point for all our receivers is given when projecting data of only the co-located imager and scintillation receiver on the same plot, a case where the mapping altitude is irrelevant. We again observe elevated σ_ϕ values primarily at the poleward edges of the aurora, as can be seen in the video

using data from only the NYA ASC and NYA scintillation receiver in the supplementary material (Video S3). Now, let us consider the case in which we project scintillation receiver data from different stations onto the same NYA ASC image. When we use, e.g., 120 km as a piercing point and projection plane for the ASC instead of 150 km, we find only very minor off-sets in relation to the auroral forms, which do not change our conclusions. As the aurorae are observed in the south of Svalbard and the ASCs, satellite positions are shown slightly further north when the piercing point and ASC projection are adjusted to a lower altitude. With this regard, mapping to an even lower altitude would only strengthen our conclusions of observing poleward elevated σ_ϕ. Note that in step 1 we vary the projections of the aurorae with the piercing point altitude, to understand how sensitive our results are when mapping all our data to different altitudes within the E-region. Whereas in step 2 we vary only the piercing point while keeping the ASC images projected to 150 km, to find whether the structuring processes happen at the same altitude as green auroral emissions.

The emission altitude of green auroral emissions is used as the piercing point altitude for the study along with ASC images of the green auroral emissions.

4.2 Case studies: spatial and temporal evolution of plasma structuring

ASC imagery of the three case study events are shown in this section. The ASC images (green aurora projected to 150 km) are plotted onto the geographical coordinates and a map of Svalbard is shown in contrast. On top of that, the observed phase scintillation data (piercing point 150 km) is displayed. The phase scintillation data is referred to as slightly elevated σ_ϕ above 0.2 rad, moderately elevated σ_ϕ above 0.3 rad, strongly elevated σ_ϕ above 0.5 rad, and very strongly elevated σ_ϕ above 0.7 rad. Not all of the measured data during, auroral activity of that day is shown: very faint aurora, forms that are not classified as part of a process showing arcs/spirals/bands, the forms that are mostly cut off by the FOV or repetitive images are excluded. The auroral activity is fluctuating in intensity and can decrease to low-intensity values or vanish shortly from the observation location before it onsets again. Whether low-intensity aurora or no aurora is observed is difficult to distinguish, as it depends on the chosen intensity scale of what will be visible. In the following, intensities measured under 10 kR-NYA/20 kR-LYR are referred to as no visible aurora. This threshold has been chosen as the elevated phase scintillation index is not observed in combination with intensities under 10 kR for NYA and 20 kR for LYR before the auroral onset. It can however be observed after the aurora vanished, this may have other reasons than auroral emissions below 10 kR/20 kR as discussed later. Only the representative images are shown in the results, but the remaining images were combined with the videos attached in the Supplementary material. Video material is available from all events as viewed from the NYA ASC and LYR ASC. The data from 22 February 2020 is also presented in form of a video recorded by the HOR ASC. In the following especially the high-intensity values of the aurora may be influenced by the way, the camera and brightness are calibrated and calculated. They are however a good measure for comparison between aurora and the σ_ϕ indices.

4.2.1 28 October 2019

The first selected event of this season occurred on 28 October 2019 (see Figs. 3a–3d). The local magnetic field B_x component shows a decrease between 18:10 and 19:30 UT measured at NYA (shown in red), LYR (green), HOP (black), BJN (orange), HOR (blue) and indicating a substorm. At HOP the magnitude of the decrease is especially large, up to a change of −600 nT in the B_x component, followed by HOR and LYR. A less severe decrease in the B_x component is observed around 20:40–21:40 UT (strongest in BJN and HOP, lightest in LYR and NYA). At the same time, the auroral activity is observed with the LYR ASC. Intense precipitation lasts from 18:15 to 19:30 UT and light precipitation from 20:45 to 21:20 UT. The latter shows only faint aurora, which is also reflected in the B_x component measurements, where we observed only light variations for LYR. Elevated σ_ϕ coincides with particle precipitation between 18:15 and 19:30 UT, this is observed for all stations. The later time interval or particle precipitation is likewise accompanied by elevated σ_ϕ, but disturbances are not in all stations recorded. BJN (Fig. 3c, shown in orange) records elevated σ_ϕ about 25 min before the strongest emissions are observed at LYR (Fig. 3b), but σ_ϕ increases right as the B_x component at BJN drops. The response of S_4 to the particle precipitation is not as clear as for σ_ϕ, but a slight increase of S_4 especially in the measurements at HOP (Fig. 3a, shown in black) may be observed around 19:00 UT. Elevated S_4 values can be an indication of diffractive effects (Yeh & Liu, 1982), but are not discussed here.

The observations on 28 October 2019 indicate a substorm event, auroral emissions, and disturbances in the phase scintillation index between around 18:10–19:30 UT and 20:40–21:40 UT (Fig. 3). This long and intense auroral activity can be best viewed from the NYA ASC as shown in Figure 4. Figures 4a–4h show a time evolution from when the auroral activity commences to when it fades out. This arc is also observed from the HOR ASC and LYR ASC. Videos of the arc from the NYA and LYR station are shown in the supplementary material (Videos S4 and S5). In Figure 4a at 18:29:23 UT light auroral activity (<30 kR) starts in the southeast quarter of the ASC's FOV, no elevation of σ_ϕ is observed at this stage. A minute later, at 18:30:23 UT, the auroral activity is at double its intensity (>60 kR) forming a faint arc. No elevation of σ_ϕ values is yet measured. At 18:31:23 UT the auroral intensity is reaching its intensity maximum (>80 kR) and now very strongly elevated σ_ϕ values are observed in the east. The delay between auroral emissions until elevated σ_ϕ values are observed is in this case 2 min, observed in LYR and NYA. The underlying processes causing elevated σ_ϕ values/plasma structuring may come with a time delay related to the recombination rates of the precipitating electrons arriving in the E-region ionosphere. The fast flows of the injected electrons could drive a two-stream instability. The difference in drift velocity between the electrons and ions, which collide with neutrals, could in specific drive the modified two-stream instability, the Farley-Buneman instability (Farley Jr., 1963). Shortly after, at 18:31:38 UT, very strongly elevated σ_ϕ values measured poleward of the established auroral arc (with an intensity still over >80 kR) are observed. Instabilities working specifically at the boundary of the particle stream may be dominant at this point, leading to very localized elevated σ_ϕ values along the poleward boundary. The intensity fluctuates

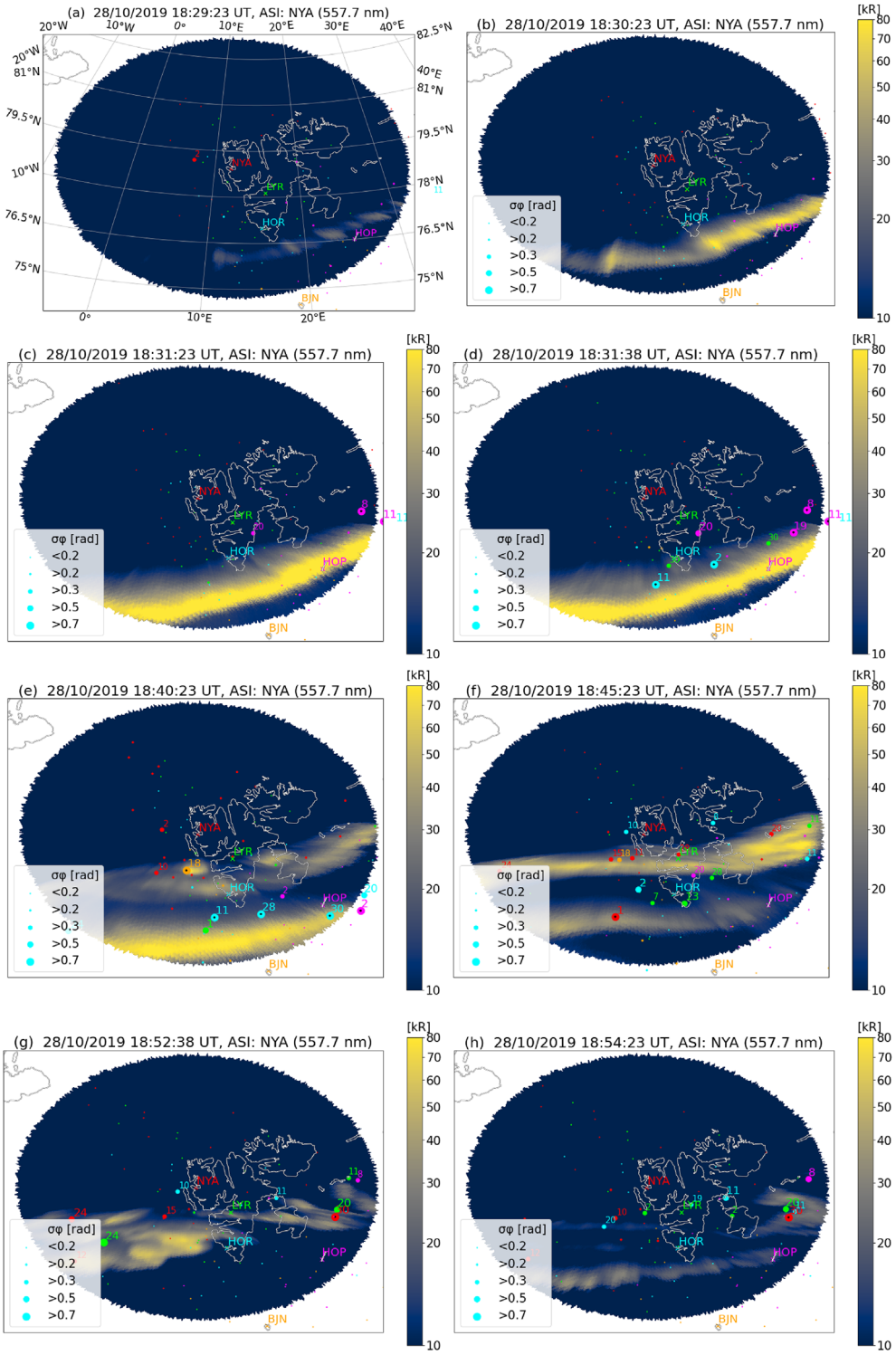

Fig. 4. The aurora shown in this figure is classified as arcs. The projection of the 557.7 nm emissions shown together with the phase scintillation index σ_ϕ over a map of Svalbard and geographical longitude/latitude on 28 October 2019 as seen from the NYA ASC for different time instances. Brighter yellow auroral emissions mean stronger intensity and bigger markers mean stronger σ_ϕ. The markers represent σ_ϕ measurements from NYA in red, LYR in green, HOR in cyan, HOP in magenta, and BJN in orange. In panel a geographic latitude and longitude gridlines are shown. The auroral intensity bar of the panel a (not shown) is the same as for the other panels in this figure. Panels a and b show the commencement of an auroral arc. Panels c and d show the arc at its maximum intensity (>80 kR). In panel d we can point out the very strongly elevated σ_ϕ poleward of the arc. Panels e and f show two auroral arcs and corresponding σ_ϕ values. Panels g and h show fading of the aurora and decrease in σ_ϕ. Even though panels a and h show similar auroral intensities (<30 kR) they show different levels of σ_ϕ: panel a – no elevated σ_ϕ, panel h – different levels of elevated σ_ϕ.

(down to <60 kR), but the σ_ϕ values stay elevated over the next 9 min. At 18:40:23 UT a second arc (with an intensity <40 kR) forms in the center of the ASC image combined with very strongly elevated σ_ϕ. The southern arc is still very intense (>80 kR) with poleward σ_ϕ values very strongly elevated. At 18:45:23 UT the arc in the center intensifies (>60 kR) and moderately elevated σ_ϕ values are observed poleward of the central arc and stronger elevated σ_ϕ values between the arcs. The southern arc has faded out (with an intensity <45 kR). At 18:52:38 UT the arc structure is dissolved and the intensity is decreased to similar values (<60 kR) as at 18:30:23 UT (before we observed elevated σ_ϕ). Occasional very strong σ_ϕ values are still observed alongside strong and moderate σ_ϕ values. This could be due to a "memory effect": the precipitation has moved away, but the E-region ionosphere has not yet restored its original state and electrons may still recombine and structures persist until the number of excess particles has declined. At 18:54:23 UT, the intensity (<30 kR) has decreased to its starting values (Fig. 4a). However occasional moderately to strongly elevated σ_ϕ values are measured. Eastwards, a low-intensity auroral patch is co-located with a very strongly elevated σ_ϕ value. The E-region ionosphere is still unstable as the structuring process continues even for weak auroral emissions.

4.3 29 January 2020

On the 29 January 2020 decreases in the local B_x component and strong auroral particle precipitation combined with increases in σ_ϕ values were observed (see Figs. 3e–3h). There are minor variations in the B_x component (about 50 nT) and light precipitation between 18:00 and 19:00 UT (Fig. 3f). After 21:50 UT fluctuations in the local B_x components are observed. The dip in B_x reaches its local minimum at a change of around −200 nT at 22:20 UT, a change much weaker than in the first studied case. Nevertheless, the auroral emissions are intense, especially around 23:00 UT. The σ_ϕ values are elevated strongly in the same time frame as precipitation is observed. The S_4 index does not show as strong a correlation to particle precipitation as σ_ϕ. In Figure 5 the event is shown as observed by the LYR ASC. In the first 30 min, the auroral activity is fluctuating and moderately elevated σ_ϕ values are found for faint aurora (<45 kR). One example is shown at 22:53:08 UT where moderately elevated σ_ϕ values are measured, but the auroral emissions are beneath (<30 kR). Whether there is a time delay in this selected case between the auroral onset and the elevated σ_ϕ values or not is difficult to determine as the auroral activity does not increase monotonically here as in the case on 28 October 2019. At 22:55:53 UT the intensity increases (>80 kR) and moderately to strongly elevated σ_ϕ values located within and surrounding the auroral form are measured. A high-intensity spiral-shaped aurora (>80 kR) is observed at 22:56:38 UT with very strongly elevated σ_ϕ. A spiral-shaped aurora has previously been linked to Kelvin-Helmholtz instability (Hallinan, 1976). The strongly elevated σ_ϕ values follow the boundary of the auroral spiral neatly, just as in Figure 4d where the elevated σ_ϕ values follow the poleward boundary of the auroral arc. At 22:57:38 UT, the auroral spiral and high-intensity area have grown. We continue to observe very strongly elevated σ_ϕ values at the boundary of the form, but now also within the form. At the boundaries of the spiral form, we observe primarily elevated σ_ϕ values poleward of the form and only rarely equatorward. A minute later at 22:58:38 UT the form has shrunk and is still surrounded by very strongly elevated σ_ϕ values. Elevated σ_ϕ values continue to be observed for over 15 min after the auroral intensity decreases below 40 kR. At 23:14:23 UT the auroral intensity is beneath 30 kR and very strongly elevated σ_ϕ values are still observed. This is another indication that there may be long-lasting structuring processes after the precipitation has declined. The observations are confirmed by the NYA and HOR cameras. The images recorded by the LYR and NYA cameras for this event are attached as Videos S1 and S6 in the supplementary material.

4.4 22 February 2020

On 22 of February multiple local negative changes in B_x, auroral emissions, and elevated σ_ϕ values are measured (see Figs. 3i–3l). In this event also S_4 is elevated, mostly in the section before 20:30 UT (Fig. 3l). The forms before 20:30 UT are very turbulent and fast moving (video of data from all three imagers shown in the Supplementary material S7, S8, and S9). The data before 20:30 UT are, due to its fast and dynamic forms, not conclusive on the spatial relation between auroral forms and elevated σ_ϕ values. Here we discuss the auroral forms after 20:30 UT as viewed from the LYR ASC. In Figure 6, at 21:00:38 UT, a band has formed in the east. The band appears fast and intense (>60 kR), with immediate strongly to very strongly elevated σ_ϕ values on the northwestward boundary of the band. No time delay between the abrupt and intense auroral onset and elevated σ_ϕ values is observed. At 21:02:08 UT the intensity has reached over 80 kR and the elevated σ_ϕ values are found in the center of the band. Here, the elevated σ_ϕ values are first observed at the boundary, but the form expands and intensifies so that the elevated σ_ϕ values move into the band-shape. Note that more GNSS satellites are crossing the band/are close to the band equatorward of HOR, but none of these are experiencing elevated σ_ϕ values. Barely any ray paths from GNSS satellites are in the band's vicinity above NYA latitudes. At 21:02:28 UT the auroral band starts fading out (<70 kR) leaving very strongly elevated σ_ϕ values poleward of the band. This is another example of how elevated σ_ϕ values are still measured for faint auroral activity. A single-point very strongly elevated σ_ϕ index can still be observed until 3 min after intense aurora. Only an auroral patch (<50 kR) is still visible in the east, here shown at 21:04:53 UT. After some minutes without strong activity, a faint auroral band (<50 kR) moves into the FOV around 21:21:53 UT, not shown in Figure 6. At 21:23:23 the form has increased its intensity to over 80 kR but only a slightly elevated σ_ϕ value is observed. Over one minute later at 21:24:38 UT the high-intensity area of the aurora grows bigger and very strongly elevated σ_ϕ values are found at the boundaries, especially poleward. Here we see again, how the auroral activity grows and expands before elevated σ_ϕ values are observed. At 21:25:52 UT the form becomes more complex, still reaching over 80 kR, and strongly to very strongly elevated σ_ϕ values are measured at the boundaries and within the form. At 21:32:38 UT (7 min later) the auroral intensity has decreased (<50 kR) and only moderately to slightly elevated σ_ϕ values are observed poleward of the band-shaped aurora. In both of the cases presented here,

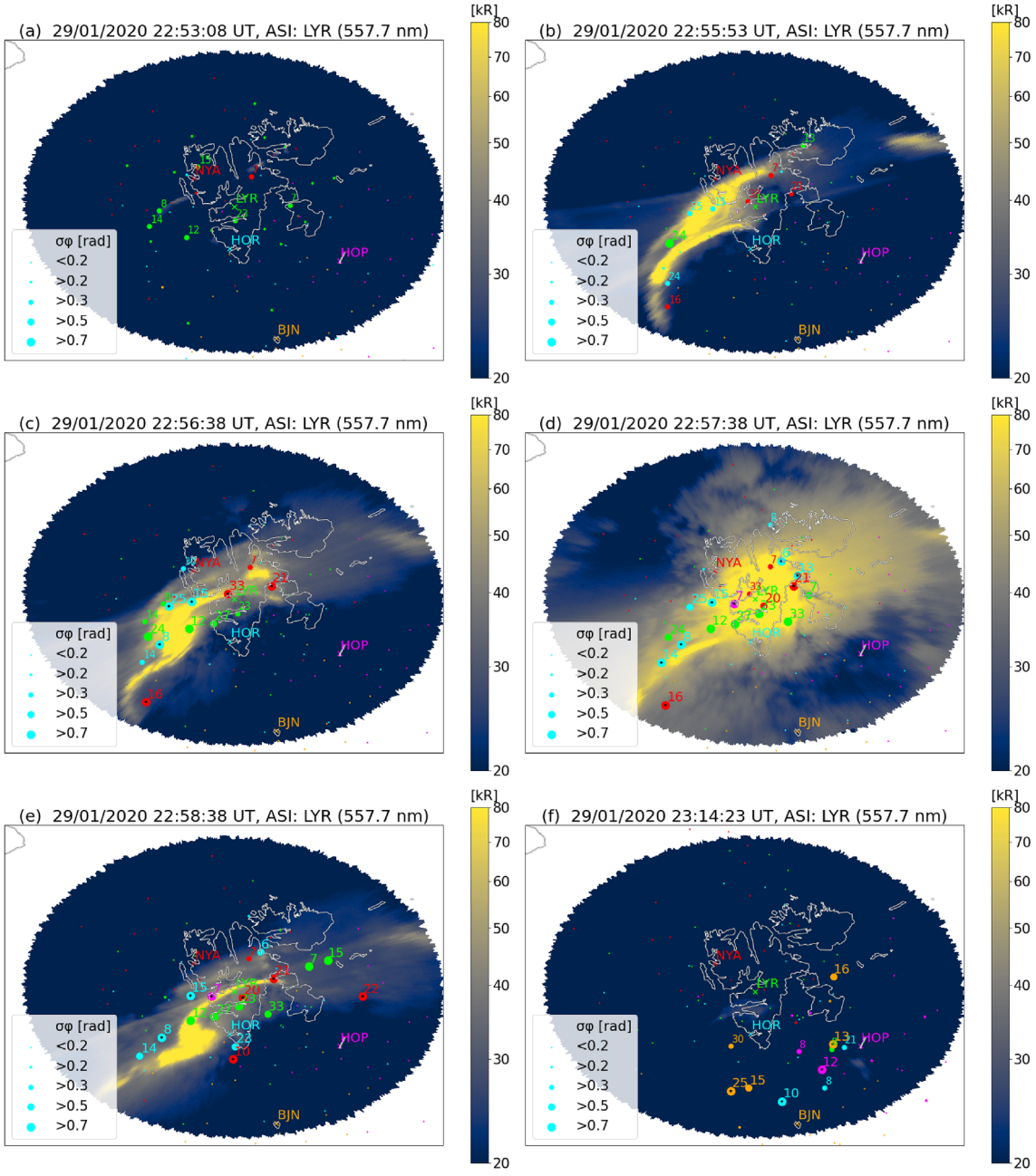

Fig. 5. The aurora shown in this figure is classified as a spiral. The projection of the 557.7 nm emissions shown together with the phase scintillation index σ_ϕ over a map of Svalbard and geographical longitude/latitude on 29 January 2020 as seen from the LYR ASC for different time instances. Brighter yellow auroral emissions mean stronger intensity and bigger markers mean stronger σ_ϕ. The markers represent σ_ϕ measurements from NYA in red, LYR in green, HOR in cyan, HOP in magenta, and BJN in orange. Panel a shows elevated σ_ϕ values yet without strong Aurora. Panel b shows strong auroral emissions and is paired with elevated σ_ϕ values. In panels c, d, and e an auroral spiral has formed and the elevated σ_ϕ values are primarily observed at the boundary of the auroral spiral. In panel f elevated σ_ϕ values on top of the faded-out form.

elevated σ_ϕ values are measured for faint aurora, suggesting plasma structuring to continue after the auroral activity has declined. On 22 February 2020 we observe fast-moving forms, and the elevated σ_ϕ values are not solely found poleward but also equatorward. As they are changing more rapidly than the other forms, the elevated σ_ϕ values may be following the auroral activity with a delay.

5 Discussion

We have studied elevated phase scintillation index values in relation to regions of auroral emission with data from three different substorm events in detail. Three distinct auroral forms were considered: arcs, spirals, and bands. While the observed arcs were stable, the other forms were more dynamic. The first

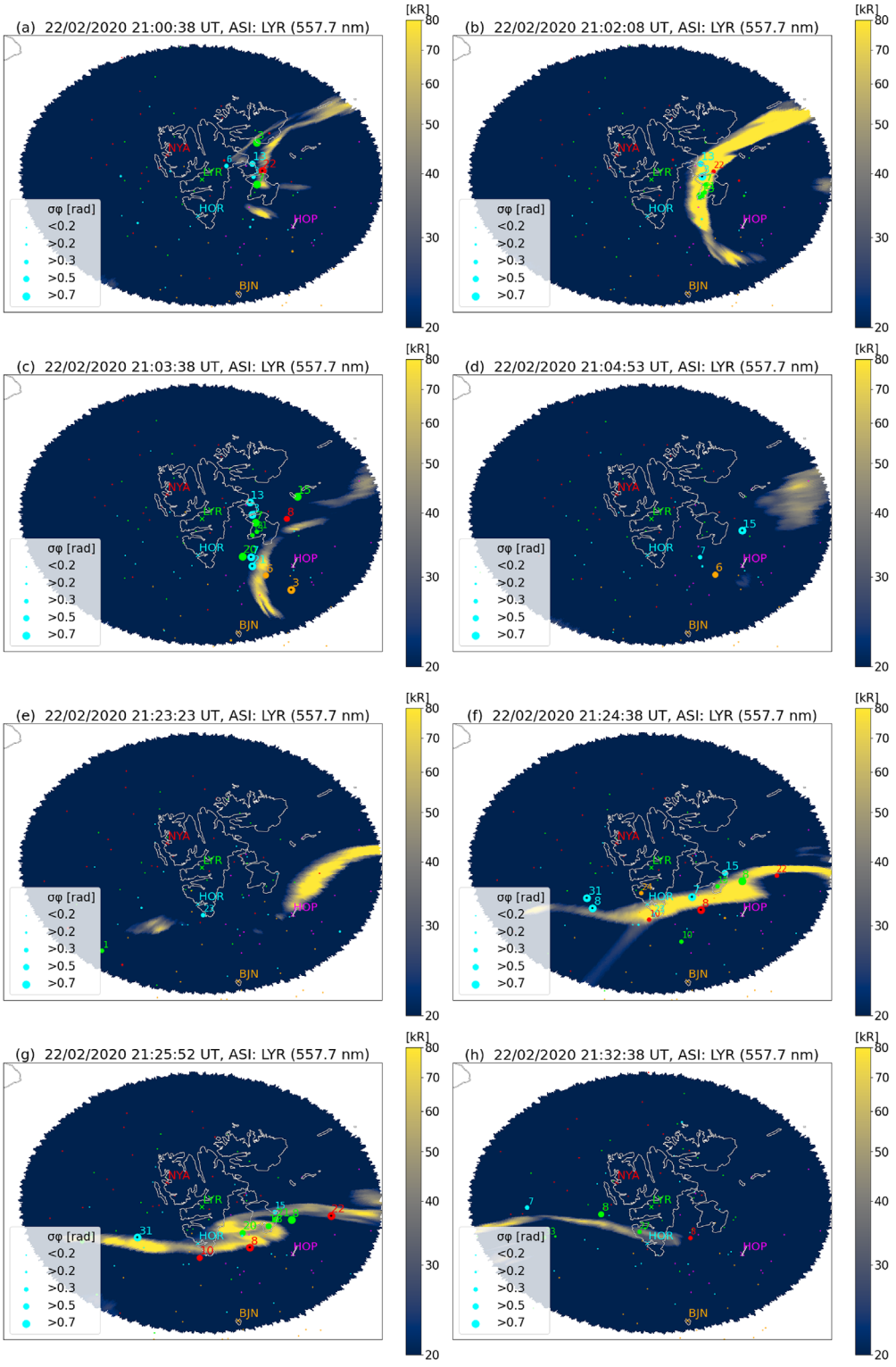

Fig. 6. The aurora shown in this figure is classified as bands. The projection of the 557.7 nm emissions shown together with the phase scintillation index σ_ϕ over a map of Svalbard and geographical longitude/latitude on 22 February 2020 as seen from the LYR ASC for different time instances. Brighter yellow auroral emissions mean stronger intensity and bigger markers mean stronger σ_ϕ. The markers represent σ_ϕ measurements from NYA in red, LYR in green, HOR in cyan, HOP in magenta, and BJN in orange. Panel a shows a band-shaped Aurora and elevated σ_ϕ values west-ward. Panel b shows the intensified band, no with even stronger σ_ϕ values. Panels c and d show the fading of the auroral band, however σ_ϕ is still elevated. Panel e shows the commencement of the next auroral band, yet without strong elevated σ_ϕ values. Panels f and g show stronger auroral emissions paired with elevated σ_ϕ values at the boundary of the auroral band. In panel h elevated σ_ϕ is observed poleward of the fading auroral band.

selected substorm event (28 October 2019) shows arcs. For the first observed arc, we found a delay in the onset of elevated σ_ϕ values of 2 min, from when auroral activity (<30 kR) was observed (see again Figs. 4a–4c). The very strongly elevated σ_ϕ values are then observed at the poleward edge of the arc (Figs. 4d–4f) and between multiple arcs (Figs. 4e and 4f). Even for faint aurora, very strongly elevated, σ_ϕ values are measured for at least 2 min after the auroral intensity has decreased to under 60 kR, Figures 4g and 4h, the moderately elevated σ_ϕ values are observed for over 4 min after. In the substorm event on 29 January 2020, an auroral spiral was observed. For the spiral, the intensity is not monotonically increasing as it was for the arc. Moderately elevated σ_ϕ values are observed even for faint Aurora (<30 kR) (see again Figs. 5a). The elevated σ_ϕ values are observed on the edges of the auroral spiral (see Figs. 5c–5e). Over 10 min after the auroral intensity decreases under 60 kR very strongly elevated σ_ϕ values are still measured (see Fig. 5f). The last of the studied substorm events (22 February 2020) shows auroral bands. The abrupt and fluctuating intensity during the onset of the band causes auroral emissions with elevated σ_ϕ to be observed right away without a delay (see Fig. 6a). The second band first shows emissions above 60 kR and it takes over a minute to observe elevated σ_ϕ values (see Fig. 6e). For both bands, we observe elevated σ_ϕ values at the poleward boundary of the auroral form (see Figs. 6b, 6d and 6f, 6g). For the first band elevated σ_ϕ values are observed also at the west-ward boundary and within the form (see Fig. 6b). When the auroral bands fade out, elevated σ_ϕ values are still observed over 1–7 min (first and second example, respectively) (see Figs. 6c, 6d and 6g, 6h).

In summary, we observed: (1) Elevated phase scintillation index values correspond consistently well with the spatial and temporal evolution of auroral forms in the green emissions (oxygen, 557.7 nm) altitudes, which means particle precipitation into the ionospheric E-region is a driver for plasma structuring. (2) There may be a time delay between the temporal evolution of aurora (e.g., commencement and fading of auroral activity) and elevated phase scintillation index measurements. (3) The elevated phase scintillation index values are observed at the boundary of the auroral emissions (poleward for discrete and stable arcs and on all boundaries for bands and spirals).

When the ionospheric piercing point for the navigation satellites is chosen at the same altitude as the projections of the green (557.7 nm) auroral emissions, the elevated σ_ϕ values are consistently observed on the auroral edges. The same behavior is found when using only the co-located ASC and scintillation receiver (see the video with data from the NYA ASC and scintillation receiver in Supplementary material), a case where the mapping altitude becomes irrelevant. Thus we suggest the σ_ϕ values to affected at the altitude of the green auroral emissions. This means that E-region irregularities and instabilities cause observed plasma structuring. The findings are in agreement with Kinrade et al. (2013) and Semeter et al. (2017), also find a better correlation between observed elevated phase scintillation index values with the 557.7 nm auroral emissions.

Previous studies (e.g., van der Meeren et al., 2014; Jin et al., 2016) linked phase scintillation mainly to the polar cap F-region ionosphere (especially to polar cap patches and tongues of ionization). The effects of intense local particle precipitation in the auroral oval on elevated σ_ϕ have been studied and referred to as a blobs type II by Jin et al. (2016). They also state that soft F-region particle precipitation does not contribute much to plasma structuring processes in the nightside auroral region. Our findings are in agreement with this, but we, however, show that more energetic particle precipitation penetrating down to the E-region may be the main source and is found co-located with intense elevated σ_ϕ. The link between elevated σ_ϕ or phase scintillations and E-region auroral particle precipitation has also been observed by several authors (e.g., Kinrade et al., 2013; Forte et al., 2017; Loucks et al., 2017; Sreenivash et al., 2020; Datta-Barua et al., 2021; Makarevich et al., 2021).

The time delay strongly depends on the auroral dynamics with regard to auroral intensity. For a case where the aurora appears out of quiet conditions and the auroral intensity increases monotonically, the phase scintillation index values are elevated around 1 (2) minutes after the intensity reached over 60 kR (30 kR), see again the example of the auroral arc or the second auroral band. This is at a level on which simultaneous and co-located aurora and phase scintillation index enhancements are commonly found, even without further increases to higher intensity levels. The duration time delay depends strongly on which intensity is used as a threshold. When the auroral intensity is increasing (decreasing) non-monotonically, the time delay maybe even longer (shorter). In the case of the spiral, or, the first auroral band considered, the elevated σ_ϕ is observed right after a prompt increase in auroral intensity.

As the auroral intensity decreases monotonically, elevated σ_ϕ is observed down to levels of under 20 kR. Especially when the auroral intensity is fluctuating around these levels, we observe occasionally highly elevated scintillation index values. We have observed elevated σ_ϕ between 1 to over 7 min after auroral intensities dropped back under 60 kR. The effect of a time delay after decreasing auroral emissions is stronger than the time delay of the elevated σ_ϕ value onset. Both may only be reached for certain conditions. For stable forms, the relation may be more clear than for dynamic forms.

Particle precipitation is a signature observed as a part of field-aligned currents (Carter et al., 2016; Xiong et al., 2020). They couple the magnetosphere to the ionosphere and can cause severe phase scintillations through direct driving of the ionospheric plasma by structured precipitation or electric fields resulting in elevated scintillation index values (Boström, 1964; Fæhn Follestad et al., 2020). Particle precipitation is usually observed in times of high convection and convection patterns were investigated with SuperDARN. We see a two-cell pattern (during southward Bz) for the studied dates. We do not observe strong flows on the nightside, and experience mostly growth in the cells, linking to dayside reconnection (Dungey, 1961; Juusola et al., 2014). The negative By component is prominent for 29 January 2020, peaking at 22:00 UT the time we observe the spiral form, and is driving an asymmetric ionospheric convection pattern (e.g., Weimer, 1995). During times of particle precipitation, the twin cell convection pattern covers Svalbard and with this precipitation area.

We propose that the time delay may occur through a "memory effect". Particle precipitation into the ionospheric E-region enhances conductance and causes a widespread irregularity dissipation and redistribution of energy (e.g., Ivarsen et al., 2021). The influx of particles increases the plasma density

leading to ionization and prolonging recombination. When the particle precipitation declines or moves, it will still take some time for plasma structures to diffuse. The structuring process initiated during particle precipitation will carry on. Instabilities in the plasma leading to further structuring processes, irregularity dissipation, and redistribution of energy.

The location of the elevated phase scintillation index values is also dependent on the spatial and temporal auroral dynamics. When investigating a stable discrete auroral form, such as the arc, we observe strongly elevated σ_ϕ (>0.5 rad) solely at the poleward boundary. If the form is faster moving, such as for spirals or bands, elevated σ_ϕ may be seen even westward or equatorward, but nevertheless on the boundaries. Fast-moving forms may move away quicker from the measurement location while elevated σ_ϕ value are still observed at this location. For spirals and bands, elevated σ_ϕ are observed also on the east and westward boundaries as well as on the boundaries within the shape. Semeter et al. (2017) studied the loss of lock (LL) events and their correlation with discrete auroral emissions. They studied mostly fast-moving auroral forms, and found LL events on equatorward (trailing) edge of the auroral form while the form is moving poleward. This agrees with our results, as we propose that there is a time delay in the elevated scintillation index measurements. Therefore, for fast-moving poleward forms, the LL events would be observed equatorward as the form moved past the measurement location further poleward. They note that although the poleward side of the arc has a similar or even greater density gradient, no LL events were observed there. This explanation may be valid in our case, as we propose that the structuring process in fact happens poleward, but the fast-moving form has simply moved from its original place as the structuring persists. This however would not explain the cases where we observe poleward elevated σ_ϕ values at multiple stable arcs, as the equatorward edge of the most poleward arc has a higher density gradient than the poleward boundary of an equatorward arc. Unless the equatorward arcs are sufficiently more intense than the poleward arcs, then the density gradient would be higher on the poleward edge of equatorward arcs (see Figs. 4e and 4f with two arcs).

The energy source for driving instabilities in the E-region ionosphere can be manifold, such as from flow shears, from gradients, or directly by kinetic energy. Instabilities associated with particle precipitation are, e.g., kinetic instabilities and two-stream instabilities. The flow of particles in field-aligned currents can also produce current-driven instabilities (e.g., Kropotkin, 2016).

One instability that can be directly produced by a velocity shear (by particle precipitation/electron beam) along the direction of or perpendicular to an externally imposed magnetic field is the Kelvin-Helmholtz instability (D'Angelo & Goeler, 1966; Hallinan & Davis, 1970; Pécseli, 2020). It can drive curls or spirals as observed in the aurora (Hallinan & Davis, 1970).

Another relevant instability that may explain the observed plasma structuring is the Farley-Buneman instability (Buneman, 1963; Farley Jr., 1963; Treumann, 1997). The instability arises from the difference in the electron and ion velocity, caused by collisions of the ions with neutrals (Farley Jr., 1963). These conditions are given in the equatorial and polar E-region ionosphere, where this instability is typically found (Rogister & D'Angelo, 1970; Pécseli, 2020).

Various instabilities can arise in the ionosphere driven by e.g., currents, energetic particle streams, or density gradients. However, the Kelvin-Helmholtz and Farley-Buneman instability do not only satisfy the encountered background conditions (E-region ionosphere, particle stream, collisions, availability of neutrals), but could also explain the observed behavior of elevated σ_ϕ observations at the edges of different auroral forms (spirals, arcs, bands) the boundaries between the injected particles and the ionospheric E-region plasma.

The Kelvin-Helmholtz instability is extracting energy out of a shear flow along a boundary (Treumann, 1997) and is associated with auroral spirals (Hallinan & Davis, 1970). This may explain why we measure elevated σ_ϕ values on the outer boundaries and boundaries within auroral spirals. The Farley-Buneman instability provides a more general explanation for plasma structuring observed at boundaries of different auroral forms, not only spirals. The auroral form boundaries are where the electrons stream past ions, which collide with neutrals, which is what feeds the Farley-Buneman instability (Buneman, 1963; Farley Jr., 1963). While the Kelvin-Helmholtz instability is working on bigger scales, the Farley-Buneman instability is operating on smaller scales. Multiple instabilities may be responsible for the plasma structuring processes we observe. Whether it is the difference in plasma density gradient that drives plasma structuring predominately at poleward edges of auroral arcs remains unknown. Further case studies with even higher spatial and temporal resolution are needed to understand the structuring process and to confirm which instability can cause delayed structuring processes in the E-region at the boundaries of auroral forms and at poleward boundaries for auroral arcs.

6 Conclusion

In this study, the relation between auroral particle precipitation and plasma structuring was investigated. In summary, the temporal and spatial evolution of auroral forms and phase scintillation index values were studied. For this, three-event days with similar background conditions (substorm events, particle precipitation, and nightside events) showing clear strong auroral emissions were selected. Data were available from three ASI imagers (NYA, LYR, and HOR) and five scintillation receivers (NYA, LYR and HOR, HOP, BJN). This provides us with 18 h of data in which we observed auroral forms such as arcs, spirals, and bands. Our results show that:

1. For the cases investigated by us elevated phase scintillation index values correspond to the spatial and temporal evolution of auroral forms when an ionospheric piercing point for navigation satellites is chosen the same as the estimated green emissions (557.7 nm) altitude (150 km). This suggests that plasma structuring in the ionospheric E-region is an important driver for phase scintillations.
2. We found a time delay between the temporal evolution of aurora (e.g. commencement and fading of auroral activity) and elevated phase scintillation index measurements. Particle precipitation enhances the plasma density. When the precipitation declines or moves, it will still take some time

for the plasma structures to diffuse. Until then, instabilities will further cause the redistribution of energy and irregularity dissipation.

3. The elevated phase scintillation index values are observed at the boundary of the auroral emissions. For discrete and stable arcs elevated phase scintillation index values are predominately observed poleward and for faster-moving shapes, including spirals and bands, on the boundaries of the form. The irregularities and instabilities causing the elevated phase scintillation index values, especially in the E-region may be due to instabilities that are driven by energy at the boundary of auroral forms, such as the Kelvin-Helmholtz instability (directly produced by a velocity shear such as from particle precipitation) or Farley-Buneman instability (through fast flows at the boundaries). Plasma structuring may predominately be observed on the poleward boundary as the gradient in plasma density is larger than it is on the equatorward boundary.

The question of why plasma structuring processes in the E-region are observed specifically at the edges of auroral forms, such as spirals and bands, and at poleward boundaries for auroral arcs open. Case studies only provide insight into a few well-studied examples of the plasma structuring processes in relation to different auroral forms. Further case studies with even higher spatial and temporal resolution and larger statistical studies investigating time-delay statistics are needed to understand the structuring process. In the future, we also need to investigate further, which instabilities are related to the plasma structuring processes and how they affect trans-ionospheric radio waves.

Supplementary materials

Supplementary material is available at https://www.swsc-journal.org/10.1051/swsc/2022038/olm

The projection of the 557.7 nm emissions shown together with the phase scintillation index over a map of Svalbard. Date, receiver location, and auroral form are indicated in the file names. Brighter yellow auroral emissions mean stronger intensity and bigger markers mean stronger phase scintillation index. The markers represent phase scintillation index measurements from NYA in red, LYR in green, HOR in cyan, HOP in magenta, and BJN in orange.

Video S1: 29012020_LYR_spiral_3fps.mp4
Video S2: 29012020_LYR_spiral_red_3fps.mp4
Video S3: NYA_arc_NYAreceiver_3fps.mp4
Video S4: 28102019_NYA_arc_3fps.mp4
Video S5: 28102019_LYR_arc_3fps.mp4
Video S6: 29012020_NYA_spiral_3fps.mp4
Video S7: 22022020 HOR bands 3fps.mp4
Video S8: 22022020 LYR bands 3fps.mp4
Video S9: 22022020 NYA bands 3fps.mp4

Acknowledgements. The authors thank Bjørn Lybekk for the maintenance of the all-sky imager and scintillation receiver data. The UiB Global Navigation Satellite System Data Collection was collected under Research Council of Norway contracts 212014 and 223252. Data from Hornsund have been acquired at the Polish Polar Station Hornsund in collaboration with the Institute of Geophysics, Polish Academy of Sciences. This study is in part supported by the European Research Council, under the European Union's Horizon-2020 research and innovation programe (Grant Agreement No. 866357, POLAR-4DSpace). We thank the institutes who maintain the IMAGE Magnetometer Array: Tromsø Geophysical Observatory of UiT the Arctic University of Norway (Norway), Finnish Meteorological Institute (Finland), Institute of Geophysics Polish Academy of Sciences (Poland), GFZ German Research Centre for Geosciences (Germany), Geological Survey of Sweden (Sweden), Swedish Institute of Space Physics (Sweden), Sodankylä Geophysical Observatory of the University of Oulu (Finland), and Polar Geophysical Institute (Russia). Florine Enengl would like to thank Noora Partamies for fruitful discussions. The editor thanks two anonymous reviewers for their assistance in evaluating this paper.

References

Akasofu S-I. 1965. Dynamic morphology of auroras. *Space Sci Rev* **4(4)**: 498. https://doi.org/10.1007/BF00177092

Akasofu S-I. 1966. The auroral oval, the auroral substorm, and their relations with the internal structure of the magnetosphere. *Planet Space Sci* **14(7)**: 587–595. https://doi.org/10.1016/0032-0633(66)90043-2.

Alfonsi L, Cilliers PJ, Romano V, Hunstad I, Correia E, et al. 2016. First observations of gnss ionospheric scintillations from Demo-GRAPE project. *Space Weather* **14(10)**: 704–709. https://doi.org/10.1002/2016SW001488.

Alfonsi L, Kavanagh AJ, Amata E, Cilliers P, Correia E, et al. 2008. Probing the high latitude ionosphere from ground-based observations: The state of current knowledge and capabilities during IPY (2007–2009). *J Atmos Sol Terr Phys* **70(18, SI)**: 2293–2308. https://doi.org/10.1016/j.jastp.2008.06.013.

Basu S, Weber EJ, Bullett TW, Keskinen MJ, MacKenzie E, Doherty P, Sheehan R, Kuenzler H, Ning P, Bongiolatti J. 1998. Characteristics of plasma structuring in the cusp/cleft region at Svalbard. *Radio Sci* **33(6)**: 1885–1899. https://doi.org/10.1029/98RS01597.

Beach TL. 2006. Perils of the GPS phase scintillation index. *Radio Sci* **41(5)**. https://doi.org/10.1029/2005RS003356.

Boström R. 1964. A model of the auroral electrojets. *J Geophys Res* **69(23)**: 4983–4999. https://doi.org/10.1029/JZ069i023p04983.

Briggs B, Parkin I. 1963. On the variation of radio star and satellite scintillations with zenith angle. *J Atmos Terr Phys* **25(6)**: 339–366. https://doi.org/10.1016/0021-9169(63)90150-8.

Buneman O. 1963. Excitation of field aligned sound waves by electron streams. *Phys Rev Lett* **10(7)**: 285–287. https://doi.org/10.1103/PhysRevLett.10.285.

Carter JA, Milan SE, Coxon JC, Walach M-T, Anderson BJ. 2016. Average field-aligned current configuration parameterized by solar wind conditions. *J Geophys Res Space Physics* **121(2)**: 1294–1307. https://doi.org/10.1002/2015JA021567.

Chernyshov AA, Miloch WJ, Jin Y, Zakharov VI. 2020. Relationship between TEC jumps and auroral substorm in the high-latitude ionosphere. *Sci Rep* **10**: 6363. https://doi.org/10.1038/s41598-020-63422-9.

D'Angelo N, Goeler SV. 1966. Investigation of the Kelvin-Helmholtz Instability in a Cesium Plasma. *Phys Fluids* **9(2)**: 309–313. https://doi.org/10.1063/1.1761674.

Datta-Barua S, Llado Prat P, Hampton DL. 2021. Multiyear detection, classification and hypothesis of ionospheric layer causing GNSS scintillation. *Radio Sci* **56(12)**: e2021RS007328. https://doi.org/10.1029/2021RS007328.

Davis T. 1978. Observed characteristics of auroral forms. *Space Sci Rev* **22(1)**: 77–113. https://doi.org/10.1007/BF00215814.

Davis TN, Hallinan TJ. 1976. Auroral spirals, 1. Observations. *J Geophys Res* **81(22)**: 3953–3958. https://doi.org/10.1029/JA081i022p03953.

Deshpande KB, Bust GS, Clauer CR, Rino CL, Carrano CS. 2014. Satellite-beacon ionospheric-scintillation global model of the upper atmosphere (SIGMA) I: High-latitude sensitivity study of the model parameters. *J Geophys Res Space Phys* **119(5)**: 4026–4043. https://doi.org/10.1002/2013JA019699.

D'Onofrio M, Partamies N, Tanskanen E. 2014. Eastward electrojet enhancements during substorm activity. *J Atmos Sol Terr Phys* **119**: 129–137. https://doi.org/10.1016/j.jastp.2014.07.007.

Dungey JW. 1961. Interplanetary magnetic field and the auroral zones. *Phys Rev Lett* **6(2)**: 47–48. https://doi.org/10.1103/PhysRevLett.6.47.

Elphinstone RD, Murphree JS, Cogger LL. 1996. What is a global auroral substorm? *Rev Geophys* **34(2)**: 169–232. https://doi.org/10.1029/96RG00483.

Farley Jr. DT. 1963. A plasma instability resulting in field-aligned irregularities in the ionosphere. *J Geophys Res* **68(22)**: 6083–6097. https://doi.org/10.1029/JZ068i022p06083.

Fæhn Follestad A, Herlingshaw K, Ghadjari H, Knudsen DJ, McWilliams KA, Moen JI, Spicher A, Wu J, Oksavik K. 2020. Dayside field-aligned current impacts on ionospheric irregularities. *Geophys Res Lett* **47(11)**: e2019GL086722. https://doi.org/10.1029/2019GL086722.

Forte B, Coleman C, Skone S, Häggström I, Mitchell C, Da Dalt F, Panicciari T, Kinrade J, Bust G. 2017. Identification of scintillation signatures on GPS signals originating from plasma structures detected with EISCAT incoherent scatter radar along the same line of sight. *J Geophys Res Space Phys* **122(1)**: 916–931. https://doi.org/10.1002/2016JA023271.

Gillies DM, Knudsen DJ, Donovan EF, Spanswick EL, Hansen C, Keating D, Erion S. 2014. A survey of quiet auroral arc orientation and the effects of the interplanetary magnetic field. *J Geophys Res Space Phys* **119(4)**: 2550–2562. https://doi.org/10.1002/2013JA019469.

Hallinan TJ. 1976. Auroral spirals, 2. Theory. *J Geophys Res* **81(22)**: 3959–3965. https://doi.org/10.1029/JA081i022p03959.

Hallinan TJ, Davis T. 1970. Small-scale auroral arc distortions. *Planet Space Sci* **18(12)**: 1735–1736. https://doi.org/10.1016/0032-0633(70)90007-3.

Hey JS, Parsons SJ, Phillips JW. 1946. Fluctuations in cosmic radiation at radio-frequencies. *Nature (London)* **158(4007)**: 234–234. https://doi.org/10.1038/158234a0.

Huba JD, Hassam AB, Schwartz IB, Keskinen MJ. 1985. Ionospheric turbulence: Interchange instabilities and chaotic fluid behavior. *Geophys Res Lett* **12(1)**: 65–68. https://doi.org/10.1029/GL012i001p00065.

Ivarsen MF, St-Maurice J-P, Jin Y, Park J, Miloch W, Spicher A, Kwak Y-S, Clausen LBN. 2021. Steepening plasma density spectra in the ionosphere: The crucial role played by a strong E-region. *J Geophys Res Space Phys* **126(8)**: e2021JA029401. https://doi.org/10.1029/2021JA029401.

Ivchenko N, Blixt EM, Lanchester BS. 2005. Multispectral observations of auroral rays and curls. *Geophys Res Lett* **32(18)**: L18106. https://doi.org/10.1029/2005GL022650.

Jin Y, Moen JI, Miloch WJ, Clausen LBN, Oksavik K. 2016. Statistical study of the GNSS phase scintillation associated with two types of auroral blobs. *J Geophys Res Space Phys* **121(5)**: 4679–4697. https://doi.org/10.1002/2016JA022613.

Jin Y, Moen JI, Oksavik K, Spicher A, Clausen LB, Miloch WJ. 2017. GPS scintillations associated with cusp dynamics and polar cap patches. *J Space Weather Space Clim* **7**: A23. https://doi.org/10.1051/swsc/2017022.

Juusola L, Milan SE, Lester M, Grocott A, Imber SM. 2014. Interplanetary magnetic field control of the ionospheric field-aligned current and convection distributions. *J Geophys Res Space Phys* **119(4)**: 3130–3149. https://doi.org/10.1002/2013JA019455.

Karlsson T, Andersson L, Gillies D, Lynch K, Marghitu O, Partamies N, Sivadas N, Wu J. 2020. Quiet, discrete auroral arcs – observations. *Space Sci Rev* **216(1)**. https://doi.org/10.1007/s11214-020-0641-7.

Keiling A, Angelopoulos V, Weygand J, Amm O, Spanswick E, et al. 2009. THEMIS ground-space observations during the development of auroral spirals. *Ann Geophys* **27(11)**: 4317–4332. https://doi.org/10.5194/angeo-27-4317-2009.

Kelley MC, Vickrey JF, Carlson CW, Torbert R. 1982. On the origin and spatial extent of high-latitude F region irregularities. *J Geophys Res Space Phys* **87(A6)**: 4469–4475. https://doi.org/10.1029/JA087iA06p04469.

Keskinen MJ, Ossakow SL. 1983. Theories of high-latitude ionospheric irregularities: A review. *Radio Sci* **18(6)**: 1077–1091. https://doi.org/10.1029/RS018i006p01077.

King J, Papitashvili N. 2005. Solar wind spatial scales in and comparisons of hourly Wind and ACE plasma and magnetic field data. *J Geophys Res* **A02104**: 110. https://doi.org/10.1029/2004JA010649.

Kinrade J, Mitchell CN, Smith ND, Ebihara Y, Weatherwax AT, Bust GS. 2013. GPS phase scintillation associated with optical auroral emissions: First statistical results from the geographic South Pole. *J Geophys Res Space Phys* **118(5)**: 2490–2502. https://doi.org/10.1002/jgra.50214.

Kintner P, Ledvina B, Kintner PM, Ledvina BM. 2005. The ionosphere, radio navigation, and global navigation satellite systems. *Adv Space Res* **35(5)**: 788–811. https://doi.org/10.1016/j.asr.2004.12.076.

Kintner PM, Ledvina BM, de Paula ER. 2007. GPS and ionospheric scintillations. *Space Weather* **5(9)**: S09003. https://doi.org/10.1029/2006SW000260.

Kintner PM, Seyler CE. 1985. The status of observations and theory of high latitude ionospheric and magnetospheric plasma turbulence. *Space Sci Rev* **41(1–2)**: 91–129. https://doi.org/10.1007/BF00241347.

Knudsen DJ, Donovan EF, Cogger LL, Jackel B, Shaw WD. 2001. Width and structure of mesoscale optical auroral arcs. *Geophys Res Lett* **28(4)**: 705–708. https://doi.org/10.1029/2000GL011969.

Kropotkin A. 2016. Formation of the small-scale structure of auroral electron precipitations. *J Atmos Sol Terr Phys* **148**: 39–47. https://doi.org/10.1016/j.jastp.2016.08.009.

Loucks D, Palo S, Pilinski M, Crowley G, Azeem I, Hampton D. 2017. High-latitude GPS phase scintillation from E region electron density gradients during the 20–21 December 2015 geomagnetic storm. *J Geophys Res Space Phys* **122(7)**: 7473–7490. https://doi.org/10.1002/2016JA023839.

Makarevich RA, Crowley G, Azeem I, Ngwira C, Forsythe VV. 2021. Auroral E-region as a source region for ionospheric scintillation. *J Geophys Res Space Phys* **126(5)**: e2021JA029212. https://doi.org/10.1029/2021JA029212.

Matzka J, Stolle C, Yamazaki Y, Bronkalla O, Morschhauser A. 2021. The geomagnetic Kp index and derived indices of geomagnetic activity. *Space Weather* **19(5)**: e2020SW002641. https://doi.org/10.1029/2020SW002641.

Millward GH, Moffett RJ, Balmforth HF, Rodger AS. 1999. Modeling the ionospheric effects of ion and electron precipitation in the cusp. *J Geophys Res Space Phys* **104(A11)**: 24603–24612. https://doi.org/10.1029/1999JA900249.

Moen JI, Oksavik K, Alfonsi L, Dåbakk YR, Romano V, Spogli L. 2013. Space weather challenges of the polar cap ionosphere. *J Space Weather Space Clim* **3**: A02. https://doi.org/10.1051/swsc/2013025.

Mrak S, Semeter J, Hirsch M, Starr G, Hampton D, et al. 2018. Field-aligned GPS scintillation: multisensor data fusion. *J Geophys Res Space Phys* **123(1)**: 974–992. https://doi.org/10.1002/2017JA024557.

Nikolaeva V, Gordeev E, Sergienko T, Makarova L, Kotikov A. 2021. AIM-E: E-region auroral ionosphere model. *Atmosphere* **12(6)**: 748. https://doi.org/10.3390/atmos12060748.

Oksavik K. 2020a. Documentation of GNSS total electron content and scintillation data (60 s) at svalbard. *DataverseNO*. https://doi.org/10.18710/EA5BYX.

Oksavik K. 2020b. The University of Bergen global navigation satellite system data collection. *DataverseNO*. https://doi.org/10.18710/AJ4S-X394.

Partamies N, Juusola L, Whiter D, Kauristie K. 2015. Substorm evolution of auroral structures. *J Geophys Res Space Phys* **120(7)**: 5958–5972. https://doi.org/10.1002/2015JA021217.

Partamies N, Kauristie K, Pulkkinen TI, Brittnacher M. 2001. Statistical study of auroral spirals. *J Geophys Res Space Phys* **106(A8)**: 15415–15428. https://doi.org/10.1029/2000JA900172.

Partamies N, Syrjäsuo M, Donovan E, Connors M, Charrois D, Knudsen D, Kryzanowsky Z. 2010. Observations of the auroral width spectrum at kilometre-scale size. *Ann Geophys* **28(3)**: 711–718. https://doi.org/10.5194/angeo-28-711-2010.

Partamies N, Weygand JM, Juusola L. 2017. Statistical study of auroral omega bands. *Ann Geophys* **35(5)**: 1069–1083. https://doi.org/10.5194/angeo-35-1069-2017.

Pécseli HL. 2020. *Waves and oscillations in plasmas. Series in plasma physics*. CRC Press. https://doi.org/10.1201/9780429489976.

Prikryl P, Spogli L, Jayachandran PT, Kinrade J, Mitchell CN, et al. 2011. Interhemispheric comparison of GPS phase scintillation at high latitudes during the magnetic-cloud-induced geomagnetic storm of 5–7 April 2010. *Ann Geophys* **29(12)**: 2287–2304. https://doi.org/10.5194/angeo-29-2287-2011.

Rogister A, D'Angelo N. 1970. Type II irregularities in the equatorial electrojet. *J Geophys Res* **75(19)**: 3879–3887. https://doi.org/10.1029/JA075i019p03879.

Semeter J, Mrak S, Hirsch M, Swoboda J, Akbari H, et al. 2017. GPS signal corruption by the discrete aurora: precise measurements from the mahali experiment. *Geophys Res Lett* **44(19)**: 9539–9546. https://doi.org/10.1002/2017GL073570.

Semeter J, Zettergren M, Diaz M, Mende S. 2008. Wave dispersion and the discrete aurora: New constraints derived from high-speed imagery. *J Geophys Res Space Phys* **113**: A12208. https://doi.org/10.1029/2008JA013122.

Skone S, Knudsen K, de Jong M. 2001. Limitations in GPS receiver tracking performance under ionospheric scintillation conditions. *Phys Chem Earth Part A* **26(6–8)**: 613–621. https://doi.org/10.1016/S1464-1895(01)00110-7.

Spogli L, Cesaroni C, Di Mauro D, Pezzopane M, Alfonsi L, et al. 2016. Formation of ionospheric irregularities over Southeast Asia during the 2015 St. Patrick's Day storm. *J Geophys Res Space Phys* **121(12)**: 12211–12233. https://doi.org/10.1002/2016JA023222.

Sreenivash V, Su Y, Datta-Barua S. 2020. Automated ionospheric scattering layer hypothesis generation for detected and classified auroral global positioning system scintillation events. *Radio Sci* **55(1)**: e2018RS006779. https://doi.org/10.1029/2018RS006779.

Tanskanen E. 2009. A comprehensive high-throughput analysis of substorms observed by IMAGE magnetometer network: Years 1993–2003 examined. *J Geophys Res* **114**: A05204. https://doi.org/10.1029/2008JA013682.

Treumann RA. 1997. *Advanced space plasma physics*. Imperial College Press. https://doi.org/10.1142/p020.

van der Meeren C, Oksavik K, Lorentzen D, Moen JI, Romano V. 2014. GPS scintillation and irregularities at the front of an ionization tongue in the nightside polar ionosphere. *J Geophys Res Space Phys* **119(10)**: 8624–8636. https://doi.org/10.1002/2014JA020114.

van der Meeren C, Oksavik K, Lorentzen DA, Rietveld MT, Clausen LBN. 2015. Severe and localized GNSS scintillation at the poleward edge of the nightside auroral oval during intense substorm aurora. *J Geophys Res Space Phys* **120(12)**: 10607–10621. https://doi.org/10.1002/2015JA021819.

Wanliss JA, Showalter KM. 2006. High-resolution global storm index: Dst versus SYM-H. *J Geophys Res Space Phys* **111(A2)**. https://doi.org/10.1029/2005JA011034.

Weber EJ, Tsunoda RT, Buchau J, Sheehan RE, Strickland DJ, Whiting W, Moore JG. 1985. Coordinated measurements of auroral zone plasma enhancements. *J Geophys Res Space Phys* **90(A7)**: 6497–6513. https://doi.org/10.1029/JA090iA07p06497.1.

Weimer DR. 1995. Models of high-latitude electric potentials derived with a least error fit of spherical harmonic coefficients. *J Geophys Res* **100(A10)**: 19595–19607. https://doi.org/10.1029/95JA01755.

Wilson GR, Weimer DR, Wise JO, Marcos FA, Wilson GR, Weimer DR, Wise JO, Marcos FA. 2006. Response of the thermosphere to Joule heating and particle precipitation. *J Geophys Res* **111(A10)**. https://doi.org/10.1029/2005JA011274.

Xiong C, Stolle C, Alken P, Rauberg J. 2020. Relationship between large-scale ionospheric field-aligned currents and electron/ion precipitations: DMSP observations. *Earth Planets Space* **72(1)**: 1–22. https://doi.org/10.1186/s40623-020-01286-z.

Yeh KC, Liu C-H. 1982. Radio wave scintillations in the ionosphere. *Proc IEEE* **70(4)**: 324–360. https://doi.org/10.1109/PROC.1982.12313.

Cite this article as: Enengl F, Kotova D, Jin Y, Clausen LBN & Miloch WJ. 2023. Ionospheric plasma structuring in relation to auroral particle precipitation. *J. Space Weather Space Clim.* **13**, 1. https://doi.org/10.1051/swsc/2022038.